ELSEVIER

Combustion and Flame 133 (2003) 467–481

Combustion and Flame

A reduced chemical kinetic model for HCCI combustion of primary reference fuels in a rapid compression machine

Shigeyuki Tanaka*, Ferran Ayala, James C. Keck

Sloan Automotive Laboratory, Massachusetts Institute of Technology, Cambridge, MA 02139

Received 2 August 2002; received in revised form 13 February 2003; accepted 20 February 2003

Abstract

A model for the Homogeneous Charge Compression Ignition (HCCI) of Primary Reference Fuels (PRFs) in a Rapid Compression Machine (RCM) has been developed. A reduced chemical kinetic model that included 32 species and 55 reactions was used and the affect of wall heat transfer on the temperature of the adiabatic core gas was taken into account by adding the displacement volume of the laminar boundary layer to the cylinder volume. A simple interaction between *n*-heptane and *iso*-octane was also included. The results showed the well-known two-stage ignition characteristics of heavy hydrocarbons, which involve low and high temperature cycles followed by a branched chain explosion. The first stage energy release decreases and the ignition delay increases nonlinearly with increasing octane number and decreasing the initial pressure. The energy release rate and total energy released were determined primarily by the rate of CO oxidation during the explosive phase following the ignition delay. The model reproduced the pressure curves obtained in the RCM experiments over a wide range of conditions remarkably well and was very sensitive to the fuel structure, the mixture composition and the initial temperature and pressure. Thus, the model can be easily adapted for predicting "knock" in spark-ignition engines and ignition-delays and burning rates in HCCI engines.

Keywords: HCCI; Reduced chemistry; Rapid compression machine; PRF; n-heptane; iso-octane

1. Introduction

The homogeneous charge compression ignition (HCCI) of hydrocarbon-air mixtures has been the subject of numerous prior experimental and theoretical investigations [1–8]. These investigations show that for heavy hydrocarbons, the ignition is a two-stage process involving a low temperature cycle followed by a high temperature cycle. Hu and Keck [1] have developed a reduced chemical kinetic model for the oxidation of primary reference fuels, which has been remarkably successful in predicting "knock" thresholds in spark-ignition engines. However, the reduced chemistry used includes only the low temperature reactions required to describe the ignition process and cannot describe the complete combustion process responsible for the major energy release.

In the present work, the Hu and Keck model has been extended to include additional elementary and global reactions that provide a complete description for the HCCI including the effects of wall heat transfer. The predictions of this extend model have been compared with recently reported experimental results from a rapid compression machine [9] and excellent agreement has been obtained over a wide range of conditions using acceptable values for all reaction rate-constants.

* Corresponding author. Tel.: 81-480-42-2215; fax: 81-480-42-3790.

E-mail address: shigeyuki_tanaka@cosmo-oil.co.jp (S. Tanaka).

0010-2180/03/$ – see front matter
doi:10.1016/S0010-2180(03)00057-9

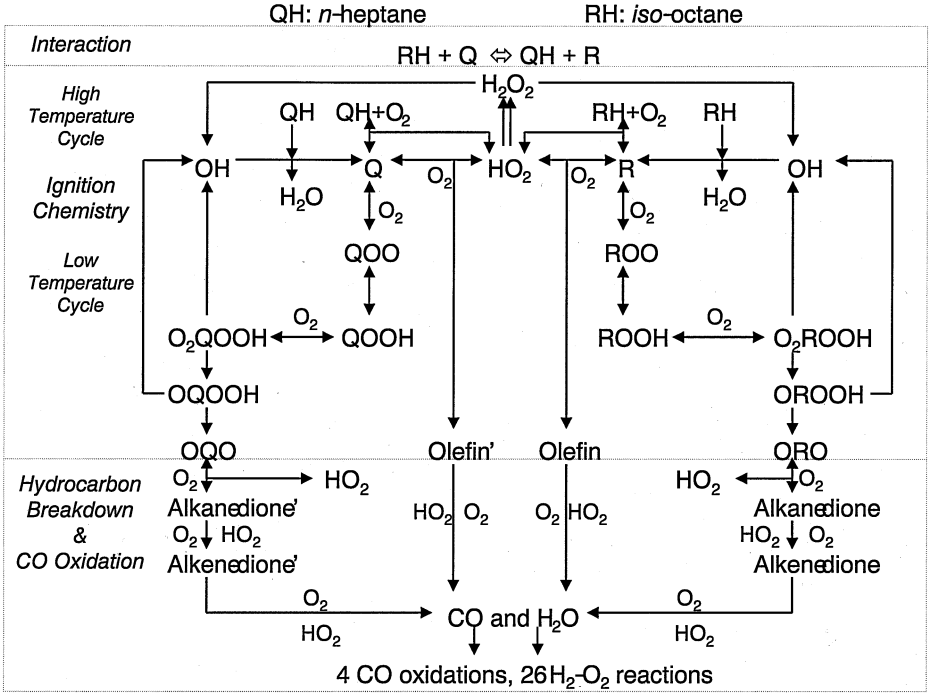

Fig. 1. Reduced-chemistry for oxidation of *n*-heptane and *iso*-octane mixtures.

2. The simulation model

The overall simulation model contains both a reduced chemical kinetic model and a thermodynamic model for the compression and heat transfer processes.

2.1. Chemical kinetic model

The reduced chemical kinetic model used contains 32 species and 55 reactions and a schematic diagram of the model is shown in Fig. 1. The calculations were performed using the CHEMKIN subroutine library [10] and the Interpreter output, which contains all the relevant input for the model, is given in the Appendix 1. The thermo chemical data for the generic species and radicals in the model were calculated using Benson group estimation technique [11] and hydrogen bond dissociation energies from the Handbook of Chemistry and Physics. The exothermic rate constants for reactions 1 to 9 and 13 to 21 were taken from [1] and the reverse rate constants were obtained from the equilibrium constants using detailed balancing. The rate constants for the global reactions R10 to R12 and R22 to R25 were adjusted to give the best fit to the experimental data from [9]. All other rate constants were taken from the CHEMKIN package.

As shown in Fig. 1, identical reaction mechanisms were used for both *n*-heptane and *iso*-octane (2,2,4-trimethylpentane). However, the rate-constants and heats of reactions for many of the individual reactions were different reflecting the very different structure of these two molecules. A coupling reaction:

$$\mathrm{RH + Q \Leftrightarrow R + QH} \quad \Delta H = +1.3\ \mathrm{kcal/mol} \quad \text{(R25)}$$

was also included. In this and following reactions QH denotes *n*-heptane, RH denotes *iso*-octane, and the heats of reaction are approximate values for *n*-heptane. (Note: the reaction numbers correspond to the reactions as they appear in Appendix 1.)

The mechanism in the case of *n*-heptane is as follows. Reaction is initiated by the abstraction of H from a fuel molecule (QH) by O_2 to form the alkyl radical Q and HO_2.

$$\mathrm{QH + O_2 \Leftrightarrow Q + HO_2} \quad \Delta H = +48.3\ \mathrm{kcal/mol} \quad \text{(R1)}$$

At low temperatures, a reversible O_2 addition reaction then occurs to produce a peroxy alkyl radical. An internal hydrogen abstraction reaction follows to form hydroperoxy alkyl radical. A second O_2 addition reaction occurs and the product decomposes irreversibly to an OH radical and ketohydroperoxide. The OH radical removes hydrogen from a fuel molecule to produce alkyl radical and H_2O. These reactions may be summarized as follows.

$$Q + O_2 \Leftrightarrow QO_2 \quad \Delta H = -32.8 \text{ kcal/mol} \tag{R2}$$

$$QO_2 \Leftrightarrow QOOH \quad \Delta H = +9.7 \text{ kcal/mol} \tag{R3}$$

$$QOOH + O_2 \Leftrightarrow OOQOOH$$

$$\Delta H = -32.8 \text{ kcal/mol} \tag{R4}$$

$$OOQOOH \Rightarrow OQOOH + OH$$

$$\Delta H = -29.9 \text{ kcal/mol} \tag{R5}$$

$$QH + OH \Rightarrow Q + H_2O \quad \Delta H = -21.9 \text{ kcal/mol} \tag{R6}$$

These are followed by the following reaction:

$$OQOOH \Rightarrow OQO + OH \quad \Delta H = +42.3 \text{ kcal/mol} \tag{R7}$$

Adding R2 through R6 leads to the highly exothermic low temperature cycle:

$$QH + 2O_2 \Rightarrow H_2O + OQOOH$$

$$\Delta H = -107.7 \text{ kcal/mol}$$

During the low temperature cycle, the temperature rises rapidly until the competing reaction:

$$Q + O_2 \Leftrightarrow \text{Olefin} + HO_2$$

$$\Delta H = -15.2 \text{ kcal/mol} \tag{R8}$$

becomes faster than reaction (R2). This is followed by the reaction:

$$HO_2 + HO_2 \Rightarrow H_2O_2 + O_2$$

$$\Delta H = -38.5 \text{ kcal/mol} \tag{R46}$$

which can be combined with R1 and R7 to form a much less exothermic high temperature cycle:

$$QH + O_2 \Rightarrow \text{Olefin} + H_2O_2 \quad \Delta H = -5.4 \text{ kcal/mol}$$

Thereafter, the temperature continues to rise slowly until the reaction

$$(M) + H_2O_2 \Rightarrow OH + OH + (M)$$

$$\Delta H = +51.3 \text{ kcal/mol} \tag{R47}$$

become important and a thermal explosion is initiated.

The above 10 elementary reactions (R1 through R8, R46, and R47) are the basis of the Hu and Keck model [1]. As can be seen, they lead to the formation of the intermediates OQO and Olefin, which were the major "products" in the Hu and Keck model. In the present work, the following additional reactions have been included to describe the oxidation process of these "products".

Table 1
Specifications of rapid compression machine

Cylinder Bore Radius (r)	25.40 mm
Clearance Height (h_2)	6.388 mm
Clearance Volume	12.95 cm^3
Stroke	95.82 mm
Compression Ratio	16.0

$$OQO + O_2 \Leftrightarrow \text{Alkanedione} + HO_2 \tag{R9}$$

$$HO_2 + \text{Alkanedione} + O_2 \Rightarrow H_2O_2 + \text{Alkenedione} + HO_2 \tag{R10}$$

$$HO_2 + \text{Alkenedione} + 5O_2 \Rightarrow 7CO + 5H_2O + HO_2 \tag{R11}$$

$$HO_2 + \text{Olefin} + 7O_2 \Rightarrow 7CO + 7H_2O + HO_2 \tag{R12}$$

Note that the rates of the 3 global reactions, R10, R11, and R12, which produce CO and H_2O, are assumed to be controlled by the reaction rate of the major second stage radical, HO_2, with relatively stable intermediate hydrocarbons. It has also been assumed that HO_2 is reproduced in these reactions. This completes the hydrocarbon oxidation mechanism, which involves each 12-reaction for *n*-heptane and *iso*-octane and 25 reactions for PRF mixtures when the coupling reaction R25 is included. The remaining 30 reactions are the standard set for the H_2 and CO oxidation [12,13].

2.2. Compression and heat transfer model

Details of the rapid compression machine used to obtain the data analyzed in this work may be found in reference [9]. Relevant parameters are given in Table I. The compression and heat transfer models are summarized in Fig. 2.

In the compression model, it is assumed that the piston moves at constant velocity, u_p, until it is slowed down at the end of the stroke by high pressure generated in a pin and groove stopping mechanism. At this point, marked by an inflection point in the pressure-time history, the piston starts to decelerate at a constant rate and boundary layer begins to grow. Prior to this inflection point, compression of the gases is assumed as adiabatic and reversible i.e. isentropic. It should be noted that in this work inflection points have been used to provide reference times because they can be much more precisely determined than maxima especially in the presence of noise or other small distortions of the measured pressure curves.

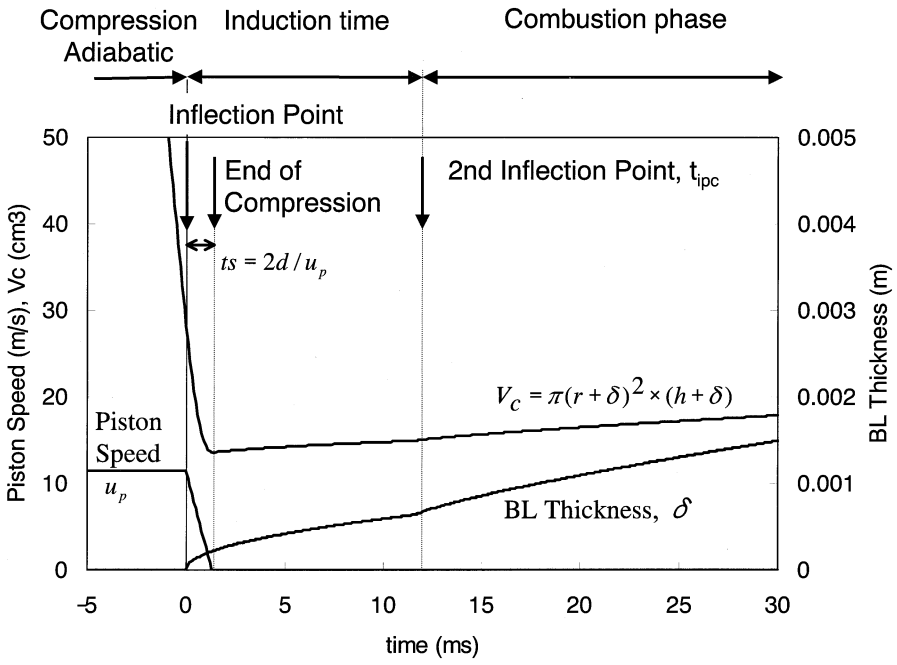

Fig. 2. Model for the compression and heat transfer in the RCM.

In the heat transfer model, it is assumed that the entire mass of gas in the cylinder is contained a uniform temperature "adiabatic core" having an effective volume, *Vc*, given by:

$$V_c = V + \delta A = \pi(r + \delta)^2 \cdot (h + 2\delta) \tag{1}$$

where V is the actual cylinder volume, A is the wall area of the cylinder, δ is the displacement thickness of the thermal boundary layer, r is the bore radius, and h is the actual cylinder height given by:

$$h = \begin{cases} h_2 + d - u_p t & : \quad t \le 0 \\ h_2 + d(1 - u_p t/2d)^2 & : \quad 0 < t \le 2d/u_p \\ h_2 & : \quad 2d/u_p < t \end{cases} \tag{2}$$

where h_2 is a clearance height between piston head and cylinder head and d is the stopping distance given by

$$d = u_p t_s / 2 \tag{3}$$

where t_s is the time between the inflection point and the peak compression pressure. Within the volume, *Vc*, the combustion process is assumed to be adiabatic. When inserted in the energy equation, the increase in *Vc* simulates the affect of an actual boundary layer on the temperature and pressure of the core gas. This method for treating heat transfer avoids the complexities associated with solving the boundary layer equations.

Prior to significant chemical energy release, it was assumed that the boundary layer was laminar and its thickness was proportional to the square root of the time, *t*, from the compression inflection point [14]

$$\delta = \sqrt{\alpha_u \cdot t} \quad (0 < t) \tag{4}$$

where α_u is thermal diffusivity adjusted to fit with the experimental compression curves for an inert gas mixture having same specific heat ratio as air/fuel mixture. Laminar heat transfer is assumed to continue until the inflection point that occurs during the major pressure rise due to combustion. At this point, a new boundary layer superimposed on the old one is assume to start in the high temperature combustion products. Thereafter the thickness of the boundary layer is represented by:

$$\delta = \sqrt{\alpha_u \cdot t_{ipc}} + (\alpha_b \cdot (t - t_{ipc}))^{\beta} \quad (t_{ipc} < t) \tag{5}$$

where t_{ipc} is the time of the inflection point and α_b and β were adjusted to fit with the experimental pressure curves after combustion.

3. Characteristic HCCI pressure curves

Typical pressure-time histories calculated from the model for fuel/air and CO_2/air mixtures having same specific heat ratios, γ, are shown in Fig. 3. In the figure, time is set equal to zero at the inflection

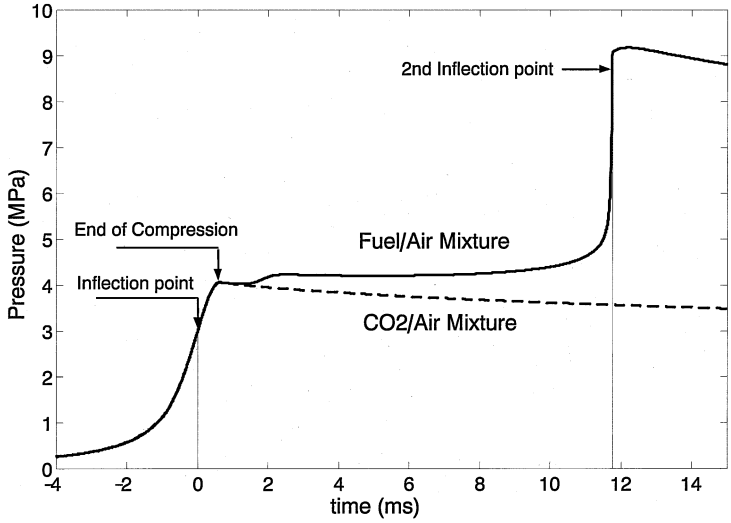

Fig. 3. An example of pressure-time history obtained in the modeling study.

point during compression. The end of compression is defined as the time at which peak pressure occurred in the air/CO_2 compression.

The pressure difference, *dP*, between the air/fuel and air/CO_2 pressure histories is shown in Fig. 4. A number of symbols used in this work are also defined. The *dPmax* is the maximum value of the *dP*. The ignition delay for the air/fuel mixtures is the difference between the time at which the *dP* reached 20% of the *dPmax* and the inflection point during compression. The ignition delay is divided into *t1* (first stage induction time) and *t2* (second stage induction time). The pressure increase during first stage is denoted *dP1*. The burn-rate for the explosive phase of combustion is the average rate of pressure increase during the time in which the *dP* rises from 20 to 80% of *dPmax*. These definitions are same as those used in reference [9].

4. Comparison of model results with experimental data

4.1. Compression and heat transfer

Figure 5 shows a comparison of the model predictions with the experimental pressure curve for

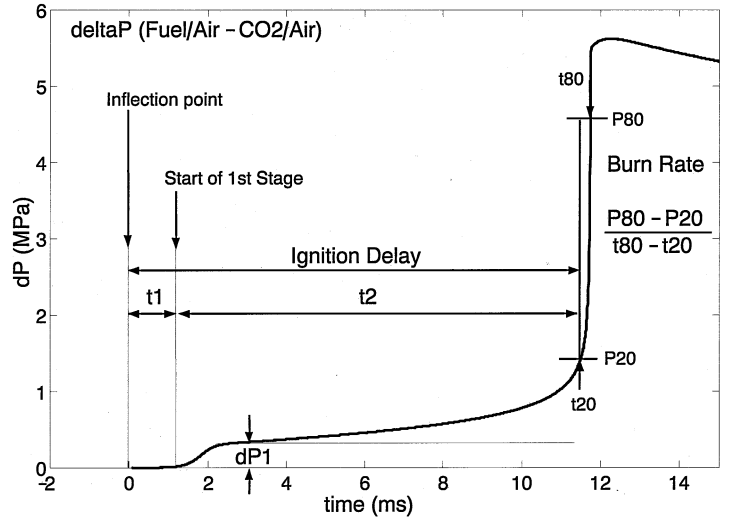

Fig. 4. Definitions of the ignition delay and the burn rate.

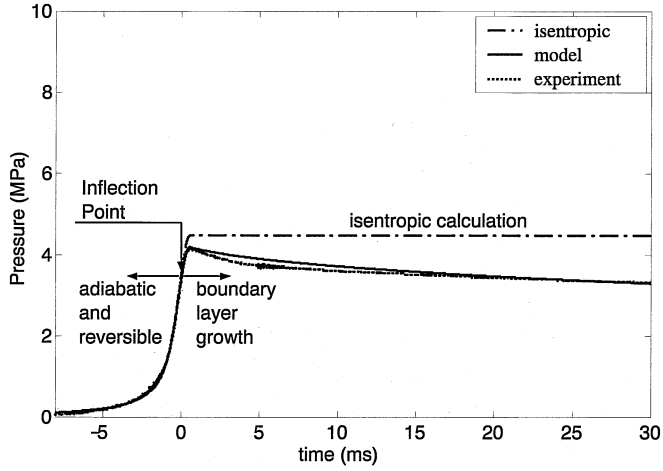

Fig. 5. The modeling of compression and heat transfer for an inert gas. Gas: Air/CO2 (14% mixture), initial temperature and pressure 318 K and 0.1 MPa, respectively. Compression Ratio: 16.

air/CO_2 (14 vol.%) mixtures. The constant piston velocity, u_p, was set to 11.5 m/s in this study. The pressure curve for isentropic compression is also shown in the figure. It can be seen that prior to the inflection point at time zero the measured and calculated curves agree perfectly. However for later times, the measured curve falls below the isentropic curve. When boundary layer heat transfer is taken into account using Eq. 4, the model calculations show good agreement with the experimental data. The values for the stopping length, d, and the thermal diffusivity, α_u, used to fit the data were 7.5 mm and 35×10^{-6} m^2/s, respectively. These values are in good agreement with the expected values based on the machine design and wall temperature.

4.2. HCCI combustion characteristics

A comparison of model calculations and experimental data for the HCCI combustion of pure *n*-heptane/air and *iso*-octane/air mixtures is shown in Fig. 6. A value of 0.8 was assumed for β and the values for α_u, α_b and t_{ipc} used to fit the data in Fig. 6 are given in Table II. It can be seen that the model calculations for both fuels show good agreement with the experimental data. Both pressure curves exhibit two-stage ignition characteristics. It can be seen that the first-stage energy release for *n*-heptane is very much higher than that for *iso*-octane leading to a very much shorter ignition delay for *n*-heptane. As well documented in reference [9], this is true for all two-stage combustion processes.

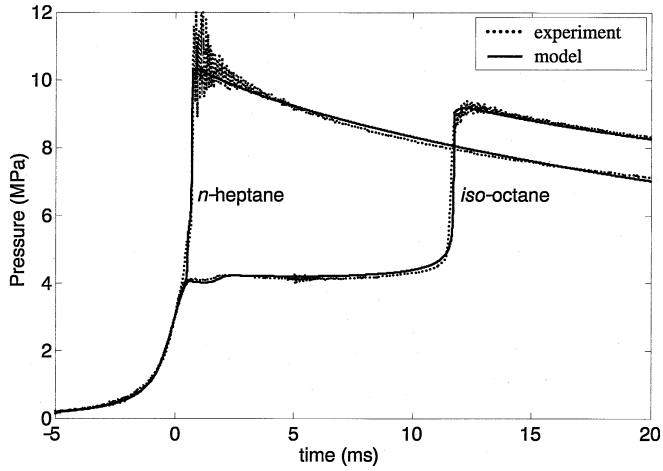

Fig. 6. The simulation results for the HCCI combustion of pure *n*-heptane or *iso*-octane. Equivalence ratio 0.4. Initial temperature and pressure 318 K and 0.1 MPa, respectively. Compression ratio: 16.

Table 2
The α_b and the t_{ipc} for each PRF/air mixture

Air/Fuel Mixture	α_u (m^2/s)	α_b ($m^{1.25}/s$)	t_{ipc} (ms)
n-heptane	35×10^{-6}	0.0150	9.07
PRF50	35×10^{-6}	0.0130	9.83
PRF75	35×10^{-6}	0.0115	11.24
PRF90	35×10^{-6}	0.0100	14.04
iso-octane	35×10^{-6}	0.0080	20.10

Equivalence ratio: 0.4, Initial Temperature: 318 K, Initial Pressure: 0.1 Mpa Compression Ratio: 16.

Model predictions and experimental data for the ignition delays and burn-rates of primary reference fuels (PRFs) are shown in Fig. 7. When the simple interaction reaction R25 is included in the model, the model simulation agrees well with the experimental data for all the PRFs included in the study. When the interaction reaction R25 is omitted, the calculated ignition delay for octane numbers other than 0 or 100 was longer than the measured value while the burn-rates were smaller.

Comparisons of model and experiment for various initial temperatures, initial pressures, equivalence ratios and octane numbers are shown in Fig. 8, 9, and 10. The initial temperatures range from 273 K to 393 K in the modeling study and from 305 K to 341 K in the experimental study. The initial pressures range from 0.075 to 0.1 MPa, the equivalence ratios range from 0.2 to 0.5, and the octane numbers from 0 to 100. The end of compression core gas temperatures were calculated using the compression and heat transfer model assuming an average value for the specific heat ratio. Agreement between experiment and theory is excellent in all cases. It can be seen that the ignition delay is strongly influenced by the octane number and the initial temperature. The equivalence ratio affected the burn rates during the explosion phase.

4.3. Sensitivity of model calculations to reaction rates

A sensitivity analysis was conducted to investigate the effect of the reaction rates on the induction times, first-stage pressure increase, and burn-rate. In all cases, the pre-exponential factor of the rate-constant for the reactions was doubled while the equilibrium constant was kept fixed. The results on the induction time and the first-stage pressure increase are shown in Fig. 11.

The first-stage induction times, *t1*, were relatively insensitive to all the reactions shown. The largest effect occurred for the second O_2 addition reactions (R4 & R16) for which the induction time was decreased by 15 percent implying that these are the rate limiting reactions for the low temperature cycle. The second-stage induction times were most strongly affected by the alkyl radical formation reactions by fuel molecule and OH radical (R6 & R18) for which the induction time was decreased by a factor of 3 and the Olefin formation reactions (R8 & R20) for which the induction time increased by a factor of 3. These same reactions also strongly affected the first-stage pressure increase but the effect was reversed. The reactions not shown in the Fig. 11 had little influence on

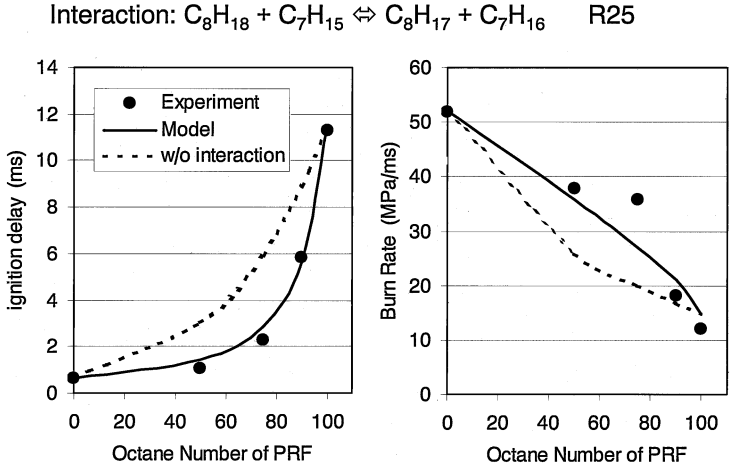

Fig. 7. The modeling results of the HCCI combustion of several PRFs. Equivalence ratio 0.4. Initial temperature and pressure 318 K and 0.1 MPa, respectively. Compression ratio: 16. The solid line is the calculated result with the reaction R25. The dotted line is the calculation result without the reaction R25.

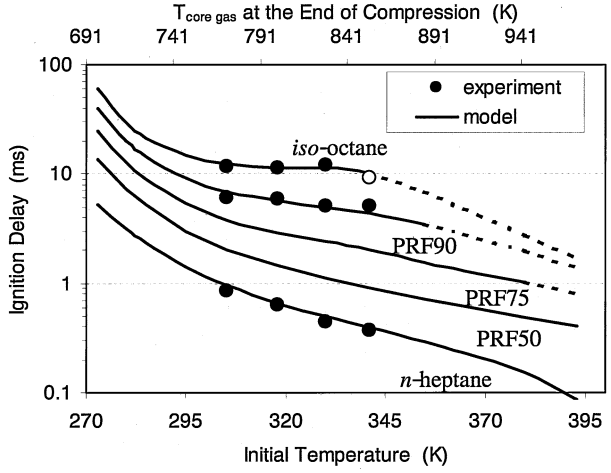

Fig. 8. The effects of initial temperature on the ignition delay. Equivalence ratio 0.4. Initial pressure 0.1 MPa. Compression ratio: 16. The open point (experiment) and the dotted lines (model) indicate that the combustion was single stage.

either the induction times or the first-stage pressure increase.

Temperature-time profiles during the HCCI combustion of several PRFs were calculated using the model and are presented in Fig. 12. It can be seen that the first-stage induction time increases as the octane number of PRFs increases while the first-stage temperature rise decreases. The temperatures at the beginning of the second-stage calculated for PRF0 (*n*-heptane), PRF50, PRF75, PRF90, and PRF100 (*iso*-octane) were 1045 K, 975 K, 923 K, 892 K, and 847 K, respectively. The ignition temperature for the thermal explosion has a constant value of around 1100 K for all PRF/air mixtures. The sensitivity of the ignition delay to the octane number can now be explained by noting that the temperature rise in the first-stage is due almost entirely to fast reactions involving the oxidation of *n*-heptane.

Pressure and temperature curves calculated for different initial pressures are shown in Fig. 13. It can be seen that the first-stage temperature rise decreases as the initial pressure decreases while the ignition delay increase. The peak temperatures at the end of compression are approximately constant while the peak pressures increase linearly with the initial pressure as would be expected from energy considerations.

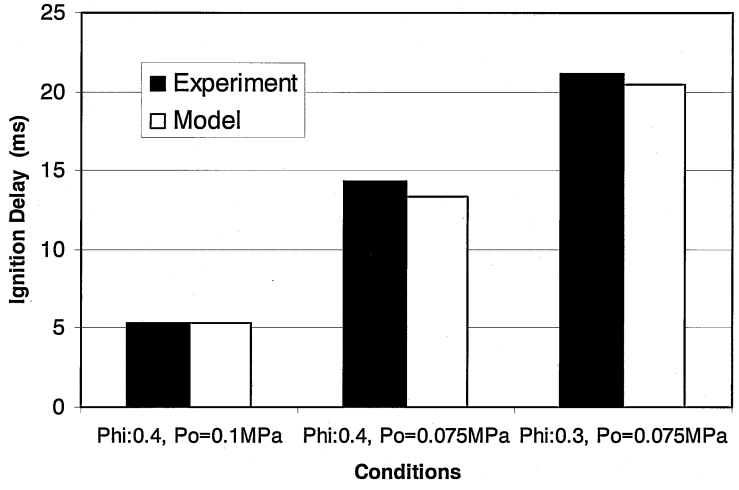

Fig. 9. The effects of initial pressure on HCCI combustion characteristics. Fuel: PRF90. Initial temperature is 333 K. Compression ratio: 16. *Phi*: Equivalence ratio. P_0: Initial pressure.

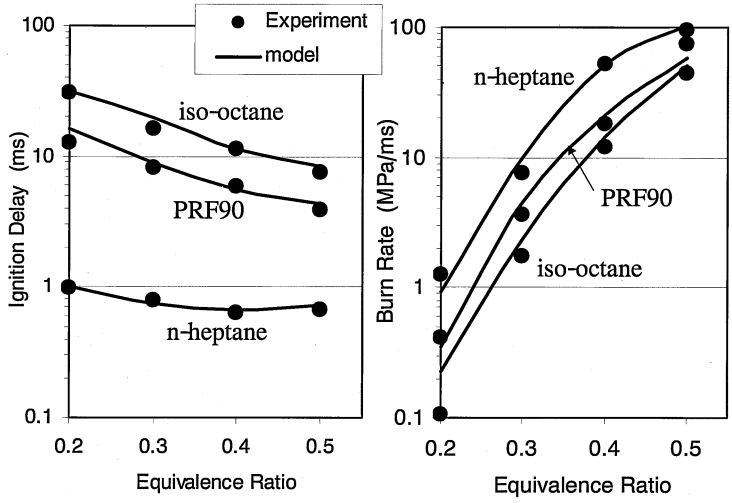

Fig. 10. The effects of equivalence ratio on the ignition delay and burn rate. Initial temperature and pressure 318 K and 0.1 MPa, respectively. Compression ratio: 16.

A sensitivity analysis for the burn rate was also conducted. The results are shown in Fig. 14. The alkyl radical formation reactions (R1 & R13, and R6 & R18) and Olefin decomposition reaction (R12 & R24) had greatest influence on the burn rate. The other reactions as well as those not shown in the Fig. 14 had little influence on the burn rate.

The calculated species profiles during the low temperature oxidation and explosion phase of the HCCI combustion are shown in Figs. 15 and 16. The major intermediate hydrocarbons formed in the first-stage low temperature cycle are Olefin, Alkanedione, and Alkenedione. During the second induction period, H_2O_2 radical are accumulated and then decompose to produce OH radicals as the temperature reaches at about 1100 K. The OH radical promote the formation of alkyl radicals, which would react with oxygen to form Olefin at high temperature. This causes the temperature to increase rapidly and Olefin decomposition occurs during the early part of the explosion phase to form CO and H_2O. Finally the CO is converted to CO_2 in the latter part of the explosion phase.

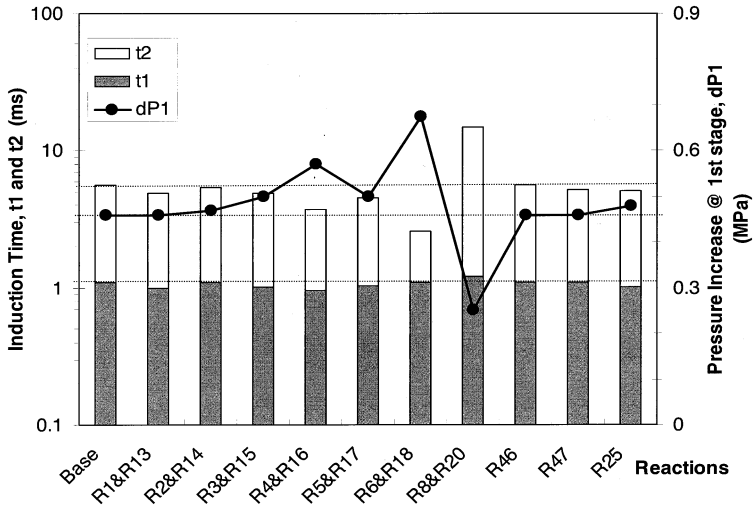

Fig. 11. The sensitivity analysis of the reactions on the ignition delay. Fuel: PRF90. Equivalence ratio 0.4. Initial temperature and pressure 318 K and 0.1 MPa, respectively. Compression ratio: 16. The dotted lines correspond to the values of *t*1, *t*2, and *dP*1 obtained with the initial set of A-factors (Base).

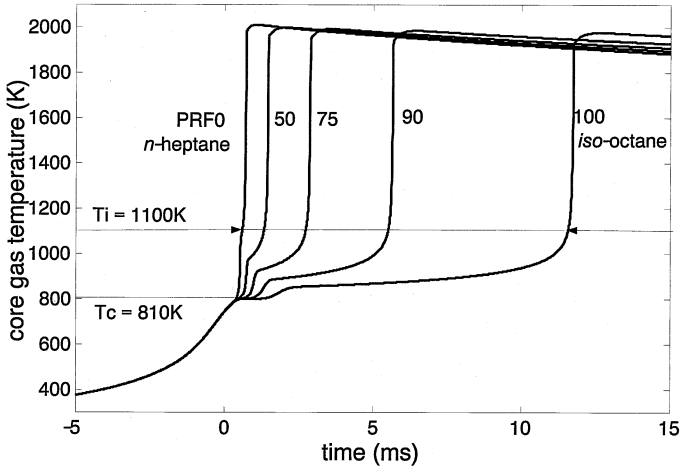

Fig. 12. The temperature time history of the HCCI combustion of several PRFs calculated using the simulation model. Equivalence ratio 0.4. Initial temperature and pressure 318 K and 0.1 MPa, respectively. Compression ratio: 16.

The CO and CO_2 profiles and the maximum temperatures (*Tmax*) calculated by the simulation model are shown in Fig. 17. Generally the CO oxidation reactions, especially CO + OH = CO_2 + H, are very slow and are strongly affected by the temperature which decreases strongly with the equivalence ratio. As a result the CO oxidation rate and corresponding energy release rate becomes very slow at low equivalence ratios. The threshold temperature for the CO oxidation is estimated to be in the range 1500 to 1600 K. This has important implications for the design of HCCI engines.

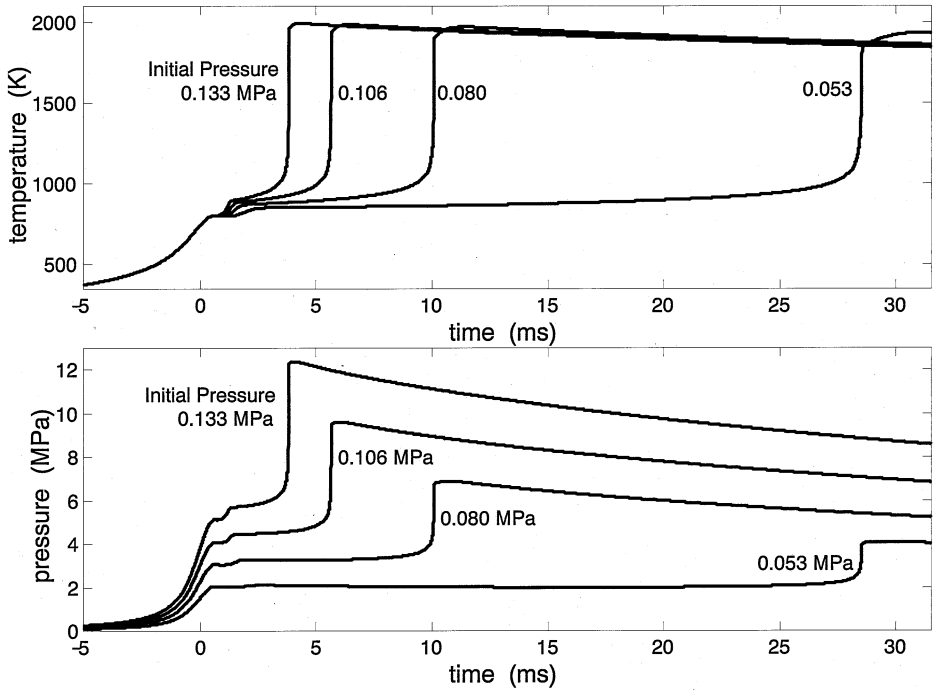

Fig. 13. The effects of initial pressure on the HCCI combustion characteristics. Fuel: PRF90. Equivalence ratio 0.4. Initial temperature 318 K. Compression ratio: 16.

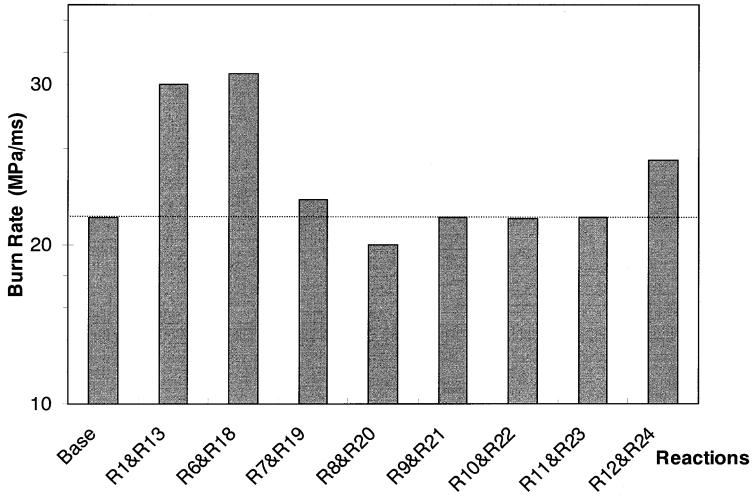

Fig. 14. The sensitivity analysis of the reactions on the burn rate. Fuel: PRF90. Equivalence ratio 0.4. Initial temperature and pressure 318 K and 0.1 MPa, respectively. Compression ratio: 16. The dotted lines correspond to the values of burn-rates obtained with the initial set of A-factors (Base).

5. Summary and conclusions

In this study, a simulation model for the HCCI combustion of *n*-heptane and *iso*-octane mixtures in a rapid compression machine was developed. The model employs reduce chemical kinetics with 32 species and 55 reactions and includes the effects of boundary layer heat transfer. The reduced kinetics includes a two-stage ignition process modeled on that of Hu and Keck with a simple interaction between

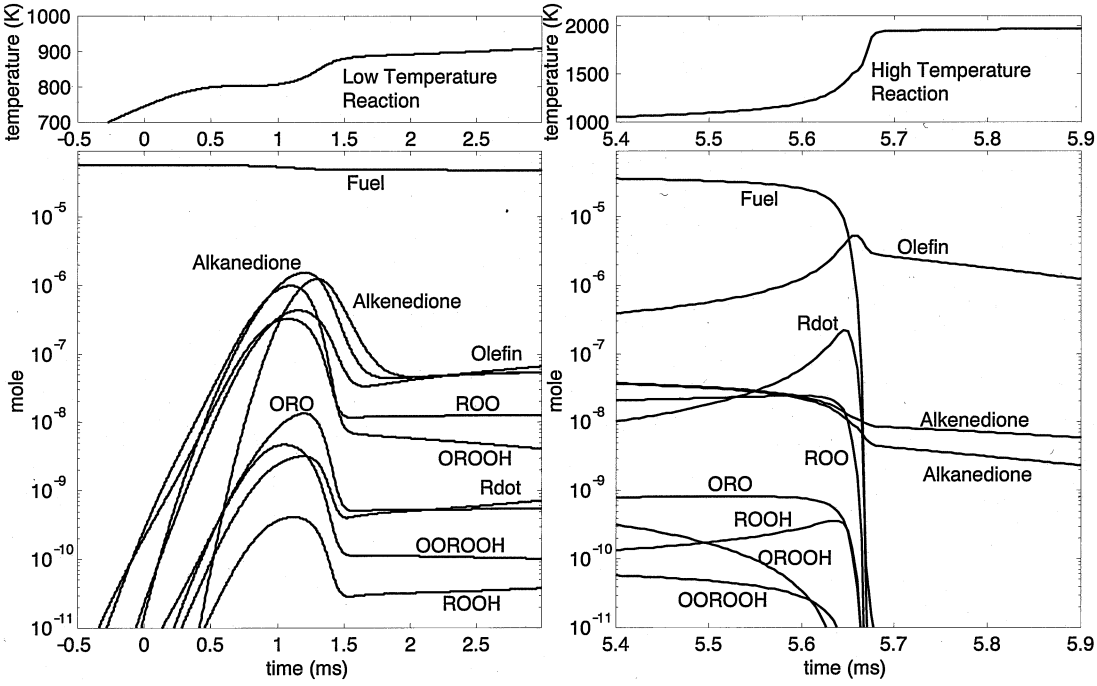

Fig. 15. The hydrocarbon species profiles during the HCCI combustion. Fuel: PRF90. Equivalence ratio 0.4. Initial temperature and pressure 318 K and 0.1 MPa, respectively. Compression ratio: 16.

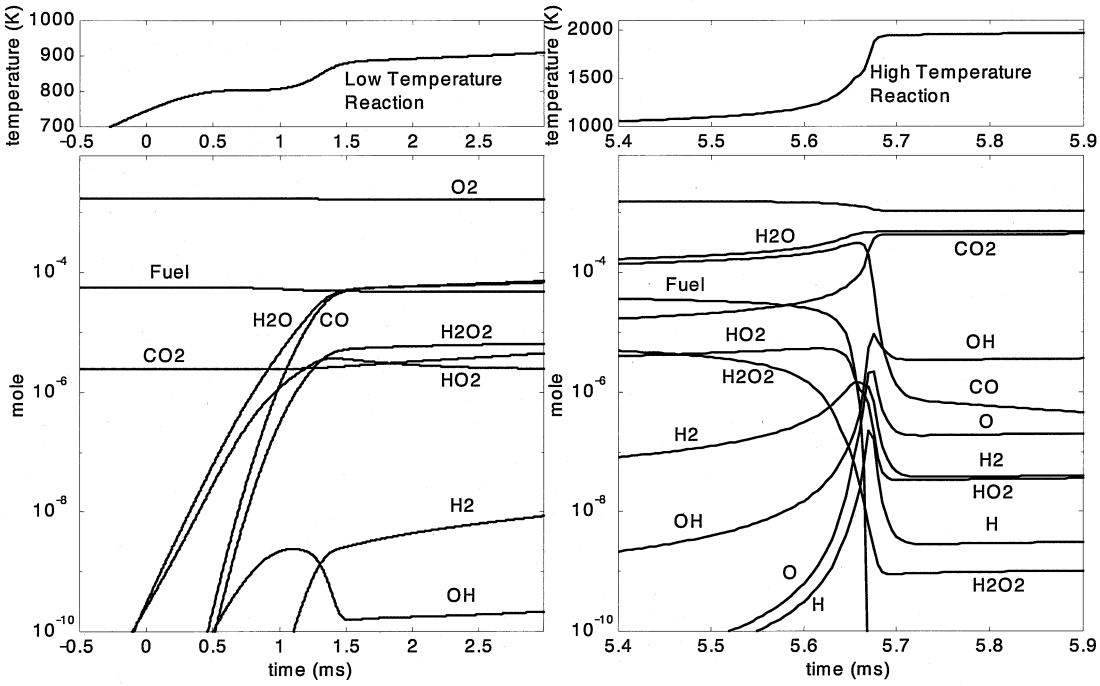

Fig. 16. The H_2-O_2 and CO oxidation reaction species profiles during the HCCI combustion. Fuel: PRF90. Equivalence ratio 0.4. Initial temperature and pressure 318 K and 0.1 MPa, respectively. Compression ratio: 16.

n-heptane and *iso*-octane, global breakdown reactions which convert intermediate products formed during the ignition stage to CO and H_2O, standard H/O chemistry, and CO oxidation reactions. The agreement between the model calculations and the experimental data over a wide range conditions was excellent. A sensitivity analysis was also performed to determine the effect of chemical reaction rates on the HCCI combustion characteristics. The following conclusions can be drawn.

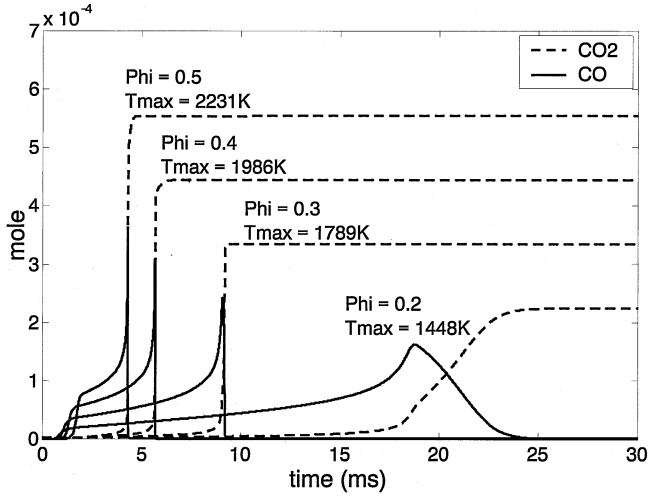

Fig. 17. CO and CO_2 profile and maximum temperature obtained from the simulation model during HCCI combustion of PRF90/air mixtures at different equivalence ratio. Initial temperature and pressure 318 K and 0.1 MPa, respectively. Compression ratio: 16.

1. The HCCI combustion of PRFs is very sensitive to the octane number.
2. The competition between the second oxygen addition and the olefin formation reactions determines the energy release during the first-stage and the ignition delay. The balance of these two reactions is very sensitive to the octane number and the initial pressure.
3. The temperature for termination of first-stage reactions increases as the octane number of PRFs decrease or the initial pressure increase.
4. The alkyl radical formation and oxidation rate of Olefin during the second-stage has a strong influence on the burn-rate during the explosion phase.
5. CO oxidation rate during the final stage of combustion and the maximum temperature at the end of combustion are strongly affected by the equivalence ratio.

Acknowledgments

The authors thank the COSMO OIL CO., Ltd and the COSMO Research Institute of Japan for their financial support and their permission to publish this article. They also wish to thank Professor John Heywood, Director of the MIT Sloan Automotive Laboratory, for his encouragement and advice and for making the facilities of the Laboratory available for this research.

References

[1] H. Hu, J. Keck, *Society of Automotive Engineers* SAE-872110 (1987).
[2] R.A. Cox, J.A. Cole, Combust. Flame 60 (1985) 109.
[3] S.W. Benson, Prog. Energy Combust. Sci. 7 (1981) 125; see also *Oxidation Communication*, 2 (1982) 169.
[4] H.J. Curran, P. Gaffuri, W.J. Pitz, C.K. Westbrook, Combust. Flame 114 (1998) 149.
[5] R.W. Walker, C. Morley, in: R.G. Compton, G. Hancock, M.J. Pilling (Eds), Comprehensive Chemical Kinetics, Vol. 35, Elsevier, New York, NY, 1997, p. 9.
[6] I. Glassman, Combustion. 3rd Ed. Academic Press, 1996 p. 84.
[7] H. Li, D.L. Miller, N.P. Cernansky, Society of Automotive Engineers SAE-960498 (1996).
[8] J. Zheng, W. Yang, D.L. Miller, N.P. Cernansky, Society of Automotive Engineers SAE-2002-01-0423 (2002).
[9] S. Tanaka, F. Ayala, J.C. Keck, J.B. Heywood, Combust. Flame (2003) 219.
[10] R.J. Kee, F.M. Rupley, J.A. Miller, CHEMKIN II: A FORTRAN Chemical Kinetics Package for the Analysis of Gas-Phase Chemical Kinetics, SANDIA Report SAND89-8009B, 1989.
[11] S.W. Benson, The Foundations of Chemical Kinetics, Robert E. Krieger Publishing Company, Florida (1982) 675.
[12] http://www.me.berkeley.edu/gri_mech. Accessed August 2002.
[13] N.M. Marinov, C.K. Westbrook, W.J. Pitz, The Eighth International Symposium on Transport Phenomena, San Francisco (1995).
[14] J.C. Keck, Letters in Heat and Mass Transfer 8 (1981) 313.

Appendix 1 CHEMKIN Interpreter Output

SPECIES

1. H_2	2. H	3. O_2	4. O	5. OH
6. HO_2	7. H_2O_2	8. H_2O	9. N_2	10. CO
11. CO_2	12. AR			
13. C_7H_{16}	14. C_7H_{15}	15. C_7H_{14}	16. $C_7H_{15}OO$	17. $C_7H_{14}OOH$
18. $OOC_7H_{14}OOH$	19. $OC_7H_{13}OOH$	20. $OC_7H_{13}O$	21. $OC_7H_{12}O$	22. $OC_7H_{10}O$
23. C_8H_{18}	24. C_8H_{17}	25. C_8H_{16}	26. $C_8H_{17}OO$	27. $C_8H_{16}OOH$
28. $OOC_8H_{16}OOH$	29. $OC_8H_{15}OOH$	30. $OC_8H_{15}O$	31. $OC_8H_{14}O$	32. $OC_8H_{12}O$

REACTIONS ($k = A\ T^n \exp(-E/RT)$)	A	n	E
n-heptane reactions			
1. $C_7H_{16}+O_2 \Leftrightarrow C_7H_{15}+HO_2$	1.00×10^{16}	0.0	46000.0
Reverse Arrhenius coefficients:	1.00×10^{12}	0.0	0.0
2. $C_7H_{15}+O_2 \Leftrightarrow C_7H_{15}OO$	1.00×10^{12}	0.0	0.0
Reverse Arrhenius coefficients:	2.51×10^{13}	0.0	27400.0
3. $C_7H_{15}OO \Leftrightarrow C_7H_{14}OOH$	1.51×10^{11}	0.0	19000.0
Reverse Arrhenius coefficients:	1.00×10^{11}	0.0	11000.0
4. $C_7H_{14}OOH+O_2 \Leftrightarrow OOC_7H_{14}OOH$	3.16×10^{11}	0.0	0.0
Reverse Arrhenius coefficients:	2.51×10^{13}	0.0	27400.0
5. $OOC_7H_{14}OOH \Rightarrow OC_7H_{13}OOH+OH$	8.91×10^{10}	0.0	17000.0
6. $C_7H_{16}+OH \Rightarrow C_7H_{15}+H_2O$	1.00×10^{13}	0.0	3000.0
7. $OCC_7H_{13}OOH \Rightarrow OC_7H_{13}O+OH$	3.98×10^{15}	0.0	43000.0

REACTIONS (k = A T^n exp(−E/RT))	A	n	E
8. $C_7H_{15}+O_2⇔C_7H_{14}+HO_2$	3.16×10^{11}	0.0	6000.0
Reverse Arrhenius coefficients:	3.16×10^{11}	0.0	19500.0
9. $OC_7H_{13}O+O_2⇔OC_7H_{12}O+HO_2$	3.16×10^{11}	0.0	6000.0
Reverse Arrhenius coefficients:	3.16×10^{11}	0.0	19500.0
10. $OC_7H_{12}O+HO_2+O_2⇒OC_7H_{10}O+H_2O_2+HO_2$	3.16×10^{13}	0.0	10000.0
11. $OC_7H_{10}O+HO_2+5O_2⇒7CO+5H_2O+HO_2$	3.16×10^{13}	0.0	10000.0
12. $C_7H_{14}+HO_2+7O_2⇒7CO+7H_2O+HO_2$	3.16×10^{13}	0.0	10000.0
iso-octane reactions			
13. $C_8H_{18}+O_2⇔C_8H_{17}+HO_2$	1.00×10^{16}	0.0	46000.0
Reverse Arrhenius coefficients:	1.00×10^{12}	0.0	0.0
14. $C_8H_{17}+O_2⇔C_8H_{17}OO$	1.00×10^{12}	0.0	0.0
Reverse Arrhenius coefficients:	2.51×10^{13}	0.0	27400.0
15. $C_8H_{17}OO⇔C_8H_{16}OOH$	1.14×10^{11}	0.0	22400.0
Reverse Arrhenius coefficients:	1.00×10^{11}	0.0	11000.0
16. $C_8H_{16}OOH+O_2⇔OOC_8H_{16}OOH$	3.16×10^{11}	0.0	0.0
Reverse Arrhenius coefficients:	2.51×10^{13}	0.0	27400.0
17. $OOC_8H_{16}OOH⇒OC_8H_{15}OOH+OH$	8.91×10^{10}	0.0	17000.0
18. $C_8H_{18}+OH⇒C_8H_{17}+H_2O$	1.00×10^{13}	0.0	3000.0
19. $OC_8H_{15}OOH⇒OC_8H_{15}O+OH$	3.98×10^{15}	0.0	43000.0
20. $C_8H_{17}+O_2⇔C_8H_{16}+HO_2$	3.16×10^{11}	0.0	6000.0
Reverse Arrhenius coefficients:	3.16×10^{11}	0.0	19500.0
21. $OC_8H_{15}O+O_2⇔OC_8H_{14}O+HO_2$	3.16×10^{11}	0.0	6000.0
Reverse Arrhenius coefficients:	3.16×10^{11}	0.0	19500.0
22. $OC_8H_{14}O+HO_2+O_2⇒OC_8H_{12}O+H_2O_2+HO_2$	1.58×10^{13}	0.0	10000.0
23. $OC_8H_{12}O+HO_2+6O_2⇒8CO+6H_2O+HO_2$	1.58×10^{13}	0.0	10000.0
24. $C_8H_{16}+HO_2+8O_2⇒8CO+8H_2O+HO_2$	2.00×10^{13}	0.0	10000.0
interaction reaction			
25. $C_8H_{18}+C_7H_{15}⇔C_7H_{16}+C_8H_{17}$	5.01×10^{12}	0.0	0.0
H_2-O_2 reactions			
26. $OH+H_2=H+H_2O$	2.14×10^{08}	1.5	3449.0
27. $O+OH=O_2+H$	2.02×10^{14}	−0.4	0.0
28. $O+H_2=OH+H$	5.06×10^{04}	2.7	6290.0
29. $H+O_2$ (+M)$=HO_2$ (+M)	4.52×10^{13}	0.0	0.0
Low pressure limit:	0.00000×10^{00}		
$0.10500\times10^{20}-0.12570\times10^{01}$			
H_2O Enhanced by 0.000×10^{00}			
H_2 Enhanced by 0.000×10^{00}			
H_2O Enhanced by 0.000×10^{00}			
H_2 Enhanced by 0.000×10^{00}			
N_2 Enhanced by 0.000×10^{00}			
30. $H+O_2$ (+N_2)$=HO_2$ (+N_2)	4.52×10^{13}	0.0	0.0
Low pressure limit:	0.00000×10^{00}		
$0.20300\times10^{21}-0.15900\times10^{01}$			
31. $H+O_2$ (+H_2)$=HO_2$ (+H_2)	4.52×10^{13}	0.0	0.0
Low pressure limit:	0.00000×10^{00}		
$0.15200\times10^{20}-0.11330\times10^{01}$			
32. $H+O_2$ (+H_2O)$=HO_2$ (+H_2O)	4.52×10^{13}	0.0	0.0
Low pressure limit:	0.00000×10^{00}		
$0.21000\times10^{24}-0.24370\times10^{01}$			
33. $OH+HO_2=H_2O+O_2$	2.13×10^{28}	−4.8	3500.0
Declared duplicate reaction...			
34. $OH+HO_2=H_2O+O_2$	9.10×10^{14}	0.0	10964.0
Declared duplicate reaction...			
35. $H+HO_2=OH+OH$	1.50×10^{14}	0.0	1000.0
36. $H+HO_2=H_2+O_2$	8.45×10^{11}	0.7	1241.0
37. $H+HO_2=O+H_2O$	3.01×10^{13}	0.0	1721.0
38. $O+HO_2=O_2+OH$	3.25×10^{13}	0.0	0.0
39. $OH+OH=O+H_2O$	3.57×10^{04}	2.4	−2112.0

REACTIONS (k = A T^n exp(−E/RT))	A	n	E
40. $H+H+M=H_2+M$	1.00×10^{18}	−1.0	0.0
H_2O Enhanced by 0.000×10^{00}			
H_2 Enhanced by 0.000×10^{00}			
41. $H+H+H_2=H_2+H_2$	9.20×10^{16}	−0.6	0.0
42. $H+H+H_2O=H_2+H_2O$	6.00×10^{19}	−1.2	0.0
43. $H+OH+M=H_2O+M$	2.21×10^{22}	−2.0	0.0
H_2O Enhanced by 6.400×10^{00}			
44. $H+O+M=OH+M$	4.71×10^{18}	−1.0	0.0
H_2O Enhanced by 6.400×10^{00}			
45. $O+O+M=O_2+M$	1.89×10^{18}	0.0	−1788.0
46. $HO_2+HO_2\Rightarrow H_2O_2+O_2$	2.00×10^{10}	0.0	5000.0
47. $H_2O_2+M\Rightarrow OH+OH+M$	1.00×10^{16}	0.0	48000.0
48. $H_2O_2+HO_2+H_2$	1.98×10^{06}	2.0	2435.0
49. $H_2O_2+H=OH+H_2O$	3.07×10^{13}	0.0	4217.0
50. $H_2O_2+O=OH+HO_2$	9.55×10^{06}	2.0	3970.0
51. $H_2O_2+OH=H_2O+HO_2$	2.40×10^{00}	4.0	−2162.0
CO oxidation reactions			
52. $O+CO\ (+M)\Leftrightarrow CO_2\ (+M)$	1.80×10^{10}	0.0	2385.0
Low pressure limit: 0.60200×10^{15} 0.00000×10^{00}	0.30000×10^{04}		
H_2 Enhanced by 2.000×10^{00}			
O_2 Enhanced by 6.000×10^{00}			
H_2O Enhanced by 6.000×10^{00}			
CO Enhanced by 1.500×10^{00}			
CO_2 Enhanced by 3.500×10^{00}			
AR Enhanced by 5.000×10^{01}			
53. $O_2+CO\Leftrightarrow O+CO_2$	2.50×10^{12}	0.0	47800.0
54. $CO+OH\Leftrightarrow CO_2+H$	4.76×10^{07}	1.2	70.0
55. $HO_2+CO\Leftrightarrow OH+CO_2$	4.76×10^{13}	0.0	23600.0

NOTE: A units mol-cm-s-K, E units cal/mol.